

利用力作用化學探討地震電磁前兆的生成機制

王錦華 王淑秋

中華民國地球科學學會

A Mechanochemical Model of Stress-induced Charges for Producing the Electromagnetic Precursors of Earthquakes

Jeen-Hwa Wang.

Institute of Earth Sciences, Academia Sinica, Nangang, Taipei, Taiwan

Abstract

The generation of ground electric charges/currents in and around a fault zone is a basic condition to produce the electromagnetic precursors before an earthquake,. Stresses loading on the fault may induce such charges/currents. Freund (2002) suggested the ‘peroxy defect theory’ to interpret the stress-induced charges. Freund et al. (2006) proposed the critical-earthquake model to explain how the underground electric currents flow in and near the epicentral area. In this study, the peroxy defect theory is studied based on mechanochemistry (Gilman, 1996). Stress-induced charges are a kind of phase transition whose reaction is controlled by the Gibbs free energy (Gibbs, 1873): $G=U+pV-TS$ in which U , p , V , T , and S are, respectively, the internal energy, pressure, volume, temperature, and entropy. G is represented by a single order parameter function. Numerical results reveal that an increase of ε makes the solution change from the stable state, then the metastable state, finally to the unstable state. In addition to the stress, the strain also influences generation of stress-induced charges. According to geometry and mechanics of stresses in the crust, the depth ranges for yielding an average normal stress which is enough to produce the electric charges are estimated. The dip angle and faulting type can influence the depth ranges that are similar for thrust and strike-slip faults, but

wider for normal faults. For the same depth range, the ability of generating electric charges is almost the same for thrust and strike-slip faults, yet lower for normal faults. The underground spatial distribution of electric resistivity may influence stress-induced currents.

Keywords Electromagnetic Precursors, Stress-induced Charges, Peroxy Defect Theory, Critical-earthquake Model, Mechanochemistry, Free energy.

1. Introduction

For earthquake prediction, electromagnetic (EM) anomalies are considered as significant earthquake precursors (Ouzounov et al., 2018; and cited references therein). The EM precursors have been observed from both ground-based instruments and satellites. The ground-based observations of EM precursors include anomalous electric resistivity and conductivity, thermal anomaly, geomagnetic fluctuations, ionospheric sounding, EM emissions, amplitude and phase anomalies of sub-ionospheric, and TEC (total electron content) anomalies. The satellites may detect wave and plasma disturbances, including the TEC fluctuations in the ionosphere above the earthquake source areas, the change of ionic composition and temperature in the ionosphere, and oscillation of the height profile of ionospheric F region.

Several models have been proposed to interpret the lithosphere-atmosphere-ionosphere (LAI) coupling for generating the EM precursors. They are: (1) a model to present radon ionization and charged aerosol and change of load resistance in the global electric circuit (Pulinets and Ouzounov, 2011; and cited references therein); (2) a model to show stressed rock-atmosphere-ionosphere coupling (Kuo *et al.*, 2011, 2014) based on stress-induced currents experimentally made by Freund (e.g., 2013); and (3) a model to display ionosphere dynamics with imposed zonal (west-east) electric field (e.g., Zolotov *et al.*, 2012; Namgaladze *et al.*, 2012).

It is necessary to find out a physical process responsible for the generation of ground electric charges/currents to meet the above-mentioned models. Numerous physical processes, including streaming potentials, piezoelectricity, piezomagnetism, triboelectricity/triboluminescence, spray, and contact electrification have been considered as the generation mechanisms. Wang (2020) took piezoelectricity as a

significant mechanism on the generation of ground electric charges.

Freund (2002) argued that those physical processes cannot represent a coherent physical model for simultaneously interpret the electrical, electromagnetic, and luminous phenomena. Freund (2000) experimentally found that water molecules embedded in rocks can dissociate into ions if the rocks are under strong stresses and the resulting charge carriers can generate currents under certain conditions. He assumed that these currents could be responsible for some EM precursors. Freund (2002) proposed the peroxy defect theory to explain experimental results. Freund and his co-authors (Freund et al., 2006; Freund and Sornette, 2007) proposed a critical-earthquake (CE) model to explain how stress-induced electric current flow in and around the source area of an earthquake. They also claimed how to apply their results to a real fault zone.

Although the experimental results and the CE model made by Freund and his co-authors sound very significant, there are still some questions. First, since the stress could not accumulate rapidly and becomes very large before an earthquake, it is questionable how to expect fast generation of large electric currents in the crust. Secondly, crustal rocks, especially in the fault zone, are usually complicated and not composed of pure rocks such as granite as used in their experiments. Hence, it is questionable to up-scale their experimental results to the real world. Thirdly, the electric resistivity, R_e , increases with depth, even though R_e is lower inside a fault zone than outside it. Unlike the expectation based on experimental results the generation of stress-induced charges decrease with increasing depth. Fourthly, the fault zone is not straightly vertical as used in the CE model and thus the dip angle and faulting type of a fault may influence the generation of stress-induced charges.

An essential problem in seismo-electromagnetic research is: Can pre-seismic slip generate the ground surface electric current? This problem is related to the physical processes, water, and rocks in the seismogenic zone. To study the problem, four issues of studies will be performed below. The first issue is the comparison between the peroxy defect theory with the seismogenic-zone structure. The second issue is to set up a working model based on mechanochemistry (Gilman, 1995) and Gibbs free energy (Gibbs, 1873) to explore the main factors in controlling generation of stress-induced charges. The third one is the construction of a lithospheric mechanical model representing the depth variations of stresses and the spatial distribution of electric resistivity in the crust to explore the possible site of source of producing p-holes and electrons proposed by CE

model.

2. Experiments and Mechanisms of Stress-induced Charges

2.1 Experiments and the peroxy defect theory

Freund (2002) proposed the peroxy defect theory to explain the experimental results about an increase in electrical conductivity in igneous or high-grade metamorphic rocks under stresses (e.g., Freund, 2011; and cited references therein). Freund and his co-workers also made valuable experiments on stress-induced charges. A simplified sided view of experimental set-up used by Freund and his co-authors is displayed in Fig. 1 in which the length of a sample and the diameter of a piston are denoted by L_s and L_p , respectively. For some experiments, the piston was located at the center of the sample. Figure 2 schematically displays the time variation in electric current. The detailed description about the experiments and theory can see Freund (2011). Only a brief explanation is given below.

Freund (2002) assumed that the activation of electronic charges (electrons and positive holes) in rocks is due to the rupture of peroxy bonds via increasing applied stresses. The positive holes are particular because they can flow outwards from the stressed rock volume into surrounding unstressed or less stressed rocks. This leads to electric currents which can travel fast and far. This leads to physical and chemical processes in a wide range around the stressed rock volume.

Figure 3 exhibits the effect of temperature, T , on the reaction of minerals plus H_2O which are denoted by ‘M’ and ‘H’, respectively. The melt, crystal, and freeze temperatures, T , are represented, respectively, by T_{melt} , $T_{crystal}$, and T_{freeze} . The solid curve plus the dashed curve represent the cooling process (from right to left) or the heating process (from left to right). The horizontal solid line whose upper bound temperature is T_{freeze} exhibits the state of freeze of minerals. Two vertical dotted lines show the temperature range around 500 °C of reduction-oxidation (redox) conversion. The solid solution, which occurs below the cooling/heating curve, is denoted by ‘SS’ and the supersaturated solid solution, which happens between the freeze line and the cooling/heating curve when $T < T_{freeze}$, is shown by ‘SSS.’

Silicates (including quartz, feldspar, mica, amphibole, pyroxene, olivine etc.) are the most common minerals in the crust and structurally composed of oxygen anions, O^{2-} , with

Si⁴⁺ or Al³⁺ (Freund, 1985, 2010). They typically have the form (X,Y)O₄ or O₃X-O-YO₃, in which X and Y are either Si⁴⁺ or Al³⁺. A type of defect occurs at the peroxy link, O₃X-OO-YO₃, where one original O²⁻ is replaced by a pair of O⁻ to form an O⁻-O⁻ bond. These defects may exhibit some particular physical properties of minerals and rocks, such as the electrical response to the applied stress and other external variables. Freund and Wengeler (1982) first observed the peroxy defects in high-purity (99.99%) melt-grown MgO single crystals. Inclusion of fluid components, for example H₂O, into the MgO matrix during crystallization makes the solute H₂O turn into OH⁻, thus yielding the defects. Around T=500 °C during cooling, the OH⁻ pairs existing at Mg²⁺ vacancy sites undergo an electronic rearrangement through a redox conversion whereby the hydroxyl protons extract one electron from their respective parent hydroxyls and then turn into H. The two respective H combine to form H₂, while the 1-valence-state hydroxyl oxygens combine to form O₂²⁻. Freund *et al.* (1982) confirmed the existence of redox conversion by replacing OH⁻ with OD⁻ in their experiments. The peroxy defects have been widely observed in silica and silicates (e.g., Freund and Masuda, 1991; Freund, 2003).

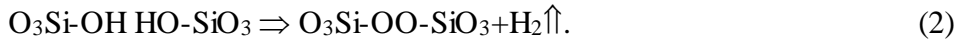
When a solid crystallizes from its melt state, a finite concentration of gas/fluid components would enter the solid matrix, thus forming a SS. The SS stability state exists in the widest range at T_{cryst} . When T decreases, the SS stability state becomes narrow. This procedure happens only through a diffusional process that allows the gas/fluid components to segregate the sub-grain boundaries and grain surfaces. At T_{freeze} , the system freezes and thus the SS becomes the SSS. This makes the system transfer from the thermodynamic equilibrium to metastability.

Under the metastable states, some reactions that cannot happen in the equilibrium conditions occur. When T decreases to ~500 °C, these hydroxyl pairs conduct a redox conversion and thus each hydroxyl proton, H⁺, steals an electron from its parent hydroxyl oxygen, O²⁻:OH⁻ ⇌ O⁻+H. Hence, the two H components combine to form a H₂; while the two O⁻ anions link together to form an O⁻-O⁻ bond. For silicates, this bond becomes a peroxy defect, i.e., O₃Si-OO-SiO₃, through the following reaction:



The redox conversion is reversible as long as the H₂ molecules remain at or close to the site where they were produced. Hence, the H₂ molecules in Eq. (1) is marked by a

subscript “i” for the meaning of ‘interstitial.’ Interstitial H₂ may diffuse away, even in dense mineral matrices. Thus, they are marked by an arrow “↑” in the following reaction equation:



Eq. (2) represents the irreversible redox conversion that happens around $T \approx 500$ °C.

Since the cooling process occurring over geological time, peroxy defects can exist in all igneous and high-grade metamorphic rocks. After those rocks upwelled from the depths to the ground surface and then eroded, peroxy defects included in detrital mineral grains, such as quartz, feldspars etc., are transported into sedimentary rocks. The minerals with peroxy bonds may change some properties (for example, the electric transport property) of sedimentary rocks. The applied stresses are highly effective in perturbing peroxy defects that are sitting at grain boundaries or bridge grain boundaries, thus causing grains to slide relative to each other. Such sliding will bend the peroxy bonds and then make them break up.

The electric charges in rocks are either ionic or electronic and thus include two types, i.e., electron (denoted as e⁻) and positive hole or p-hole (denoted as h^{*}). The latter represents a defect electron. Most of crustal rocks consisting of silicate minerals or containing detrital silicate minerals are characterized by O²⁻ anions. Some O²⁻ have released an electron and turned into O⁻. Two O⁻ atoms may be bonded together in a peroxy link and represent a pair of trapped p-holes, which are electrically inactive or in the dormant state. In other word, the h^{*} is an electronic state associated with O⁻ in a matrix of O²⁻. The peroxy bonds that are electrically inactive as they are intact can break up when they are perturbed. During break-up, one e⁻ is transferred from a neighboring O²⁻ into the broken peroxy bond in the following reaction equation:



In Eq. (3), the peroxy bond is displayed by two dots ‘:’ where a dot denotes a single- hole state. The electron is trapped in the new broken peroxy bond which is represented by a single dot ‘•’. At the same time, the O²⁻ that has released an electron turns into an O⁻. This quasi-free O⁻ represents a defect electron in the oxygen anion sub-lattice, i.e. a p-hole or

h^* .

The energy levels of unbroken peroxy defects correspond to the O 2sp-symmetry states that form the upper edge of the valence band. Likewise, new-created e' and h^* states exist at or near the upper edge of the valence band. The e' is trapped by shifting downward to new energy levels slightly below the surface of the valence band; while its conjugated mirror state (denoted by e'^*) shifts upward into the band gap, slightly above the uppermost level of the valence band. Note that the e' and e'^* states are available only at the places where the peroxy bond breaks due to external stresses. Hence, the e' is mobile only within the stressed rocks. By contrast, the h^* is associated with energy levels that form at the uppermost valence band. Since its wave-functions are highly delocalized, it can spread out from the stressed rocks.

Freund *et al.* (2006) observed that h^* is dormant in rocks subjected by deviatoric stresses. When the loading rate is the same as the tectonic stress, a rock deforms continuously with a visco-elasto-plastic bulk rheology, i.e., in the ductile regime. Most of the ductile deformations are irreversible and the grains slide relative to each other showing dislocations (in other word, in a thermally activated process). Peroxy bonds somewhat modify the grain boundaries or dislocations, and a small relative motion of mineral grains would break the O⁻-O⁻ bonds. As described by Eq. (2), the broken peroxy bonds will take over an electron from a neighboring site, for instance a nearby O²⁻ which behaves like a donor. While the electron is trapped in the broken peroxy bond, the donor O²⁻ turns into an O⁻. This equivalent to a defect electron on the O²⁻ sub-lattice, i.e., an h^* . This h^* state is not bound to the broken peroxy bond but can diffuse away via a phonon-coupled electron hopping mechanism (Shluger *et al.*, 1992) at a fast process with a speed of ~100 m/s (Scoville *et al.*, 2015). Such an h^* flows from the stressed rock to unstressed one as displayed in Fig. 1.

2.2 The Critical-earthquake model

Freund and his co-authors (Freund *et al.*, 2006; Freund and Sornette, 2007) proposed the CE model to explain how stress-induced electric current flow in and around the source area of an earthquake. They assumed that a fault zone (denoted as 'a cross section' in their paper) are collided by two crustal blocks bounded by a straightly vertical fault. Figure 4 shows the generalized seismogenic-zone structure (cf. Scholz, 1990). In their model, each block is composed of two parts (see Fig. 4). The upper crust is cooler, brittle,

and weak, and the middle-to-lower crust is hotter, ductile, and strong. Under a tectonic driving force, the two blocks are pushed against each other at a constant speed, thus leading to a constant strain before an earthquake. The stressed volume for producing charges is in the lower part of upper crust. They also assumed the existence of two important zones. The first zone is almost around the bottom of seismogenic layer in the upper crust as shown in Fig. 4. Inside this zone, rocks change from brittle to ductile due to depth-increasing T . Higher T makes rocks become more ductile in the lower crust. They also addressed that the depth of brittle-to-ductile transition zone is not fixed because a ductile response at low stresses (leading to slow deformations) may be turned into a brittle response under high stresses (resulting in rapid deformations). The second zone is below the seismogenic layer and in the lower crust. Inside this zone, the electric conductivity, C_e , changes from p-type to n-type. An n-type material has the n-type conductivity when its electric current consists of mainly electrons moving in the conduction band or on high-lying energy levels. A p-type material has the p-type conductivity when its electric current comprises defect electrons or p-holes travelling along the valence band. Since the transition can occur at a very low stress, such as 1 bar, the stress is only a minor factor in influencing the p-n transition. Freund (2007b) claimed that the p-n transition is caused mainly by the thermal activation of electrons from the valence band to the conduction band or to some high-lying energy levels. Freund (2003) stressed that in the upper crust with $T < 400$ °C, rocks slightly show p-type conductivity; while in the lower crust with $T > 500$ – 600 °C, rocks have n-type conductivity.

3. Discussion

3.1 Relationship between the peroxy defect theory and the seismogenic zone

A combination of the phase diagram (Fig. 3) and the seismogenic-zone structure leads to Fig. 4 that shows the vertical geological profile of a fault zone in the crust and upper mantle. Included also in this figure are several depths of key temperatures related to the peroxy defect theory. Since the thicknesses of related layers are of region-dependence, the exact depths are not given in the figure. The fault zone that extends from the ground surface to the depth of several to several tens kilometers (Sibson, 1977) is usually divided into three sections that are specified with different materials in different

depth ranges. Section 1 is in the depth range 0–2 km and consists mainly of clay gouges and breccias. Section 2 is the seismogenic layer and composed mainly of cataclasite from ~2 km to ~11 km or deeper. Section 3 covers almost the lower crust from the bottom of Section 2 to the bottom of the crust in a depth range between ~11 km and ~33 km or deeper. The major compositions in Section 3 are mylonites. The temperature is <100 °C in Section 1, between 100 °C and 300 °C in Section 2, and >300 °C in Section 3 (see Scholz, 1990).

Brittle ruptures usually happen in the seismogenic layer, i.e., Sections 1 and 2, consisting of cataclasites that are formed by fracturing and comminution during faulting and normally cohesive and non-foliated and is dynamically unstable. The lower crust, i.e., Section 3, being composed of mylonites that are a product of plastic deformations and flinty and finely laminated crushed rocks, has a single foliation and lineation and is dynamically stable. Thus, ductile deformations occur in the lower crust. The depth distribution of strengths, which will influence regional seismicity, is shown in the left-hand side of Fig. 4. The strength first linearly increases with depth (depicted by a solid line) because of elastic behavior and then decreases with increasing depth (exhibited by a dashed curve) due to ductile deformations. The peak strength is at the depth which is the lower boundary of brittle (or earthquake) ruptures.

The values of T_{melt} of magma are usually in the range 700–1300 °C (Anderson, 1989; Weidendorfer *et al.*, 2017). The geothermal gradient ranges from 20 to 30 °C/km (Turcotte and Schubert, 1982). Hence, the magma reservoirs exist in the upper mantle which is at the lowest depth denoted by a dashed line in the mantle part of Fig. 4. The solid solution could exist beyond the layer with $T=T_{crystal}$ which at the depth displayed by the secondly lowest dashed line in the figure. Freeze of rocks happens in the mantle beyond the depth with $T=T_{freeze}$ as shown in the figure. The redox conversion, which occurs at $T\approx 500$ °C, should appear in the depth range 16.7 to 25 km with an average depth displayed by a dashed line specified with $T=T_{re}$ in the lower crust. Two thin dotted lines represent the depth range for redox conversion. Although redox conversion occurs in the lower crust, earthquakes cannot initiate in its depth range because such a range is below the maximum rupture depth and in the regime of mylonites where only plastic deformations happen. The SSS that exists in the seismogenic zone is associated with initiation of earthquakes.

3.2 Mechanochemistry and Gibbs free energy

The peroxy defect is a phenomenon of ‘mechanochemistry’ or ‘mechanical chemistry’ that exhibits chemical reactions of solids under mechanical stresses on a molecular scale (Gilman, 1996). The mechanochemical processes are complex and radically different from usual thermal or photochemical mechanisms which are the traditional ways of dissolving, heating, and stirring chemicals in a solution. The interaction between mechanics and chemistry can decrease the gap between two energy levels, thus causing ionization of electrons and then producing chemical reactions. Mechanochemistry can happen in wear and abrasion, friction and lubrication, and stress-accelerated degradation of materials. These actions are important on nucleation and rupture processes of earthquakes and also on the generation of seismic precursors before or during the nucleation processes.

Sornette (1999, 2001) first considered mechanochemistry as one of possible mechanisms of producing earthquake precursors. The motion of a dislocation due to kink (leading to plastic deformation) is similar to a local chemical reaction in which an embedded ‘molecule’ is dissociated, and then one of the product atoms joins with an atom from another dissociation to form a new ‘molecule’ (Gilman, 1995). Chemical reactions can be triggered by mechanical forces in solid phases, because unlike gases and fluids, solids can support shear strain. Shear changes the symmetry of a molecule or a solid, thus being effective in stimulating reactions, much more so than isotropic compression (Gilman, 1996). The reason for the strained minerals to be transformed into metastable is due to the kinetic process. In order to apply the concept to the crust, it is necessary to understand the constraints in the physical parameters that may control the chemical transformations.

Figure 5 displays the plot of energy versus the wavenumber $\kappa=\pi/l$ where l is the lattice spacing of the square array of mineral lattice. The magnitude of wave-vector at the zone boundary is $2\pi/l$, and the energy of an electronic state is $E=\hbar^2\kappa^2/2m_e$, where \hbar ($=1.0545\times 10^{-34}$ J-s) is Planck's constant h ($=6.6255\times 10^{-34}$ J-s) divided by 2π , m_e is electron effective mass ($=9.11\times 10^{-31}$ kg), and $2\pi\kappa$ is the electron wavelength, λ . On the left, the energy states are shown with an energy gap at $\kappa=\pi/l$. At the mid-point of the gap, the energy level is $E_o=(h/l)^2/8m_e$. The energy gap is $E_g=2/|V_P|$, where V_P is the periodic potential energy with period, l . The dependence of E on κ in the two directions perpendicular to the sides of the square lattice is the same.

Suppose that a hydrostatic strain is applied to the square lattice. In two orthogonal directions, the atomic spacing, l , decreases and the plot of E versus κ will shift as shown on the far right in Fig. 5. The lattice spacing become $l(1-\varepsilon)$, where ε is the strain. To a first approximation, E_g does not change, but the position of the gap relative to E_o increases. The κ becomes $\pi/l(1-\varepsilon)$ at the zone boundary. Since the shifts of the band-gap mid-points are the same in the two orthogonal directions of the square lattice, the minimum band gap is not changed at the first-order approximation.

The applied shear can cause anisotropic strains: an increase in one axis and a decrease in the other. Therefore, the zone boundaries become $\kappa=\pi/l(1\pm\varepsilon)$, and the band-gap mid-points shift in opposite directions. Thus the minimum gap becomes E_g^* as indicated in Fig. 5. Note that the effect may be relatively large because of the parabolic dependence of E on κ . When the strain becomes large enough to close the gap, the bonding electrons are delocalized into the anti-bonding states. In other word, the activation energy for the reaction, or transformation, becomes zero, and it can proceed athermally. In the intermediate cases, the electronic process may be assisted by phonons. The minimum (critical) strain, ε^* , used to close the gap is about $2m_eE_gl^2/h^2$ (Gilman, 1995). Obviously, ε^* increases with E_g and l^2 . For example, the value of ε^* is $\sim 8\%$ when $E_g=2$ eV (electron volt, $1 \text{ eV}=1.602\times 10^{-12}$ erg) and $l=2.5 \text{ \AA}$ ($1 \text{ \AA}=10^{-10}$ m). It is easy to close the gap when $\varepsilon>\varepsilon^*$.

The free energy is commonly used for the study of phase transitions (see Reif, 1965). Gibbs (1873) first defined the free energy (SI unit: joule) as

$$G=U+pV-TS=H-TS \quad (4)$$

where U is the internal energy (SI unit: joule); p is pressure (SI unit: pascal); V is volume (SI unit: m^3); T is the temperature (SI unit: kelvin); S is the entropy (SI unit: joule per kelvin); and $H(=U+pV)$ is the enthalpy (SI unit: joule). Note that in thermodynamics, the internal energy of a system is the energy contained within the system and the energy necessary to create or prepare the system in any given state. But it does not include the kinetic energy and the potential energy of the system. G is the maximum amount of non-expansion work that can be extracted from a thermodynamically closed system that can exchange heat and work with its surroundings in the standard state. The maximum can be

attained only in a completely reversible process. When a system transforms reversibly from an initial state to a final state, a decrease in G is the work done by the system to its surroundings minus the work acted by the pressure. In addition, G is also the thermodynamic potential that is minimized when a system reaches chemical equilibrium at a constant T (i.e., the isothermal process) and a constant p (i.e., the isobaric process). This means $dG/dQ=0$ at the equilibrium point, and thus a reduction in G is a necessary condition for the spontaneity of processes at constant T and p .

Sornette (2001) suggested the use of Landau theory (Landau, 1937) to study phase transitions in minerals. In general, minerals and their structural phase transitions involve several coupled order parameters Q_i , which describe the atomic displacements within the lattice structure. These parameters form a tensor that couples to the strain tensor ε_{ij} . To simplify the problem, Sornette (2001) used the simplest conceptual model of a coupling between a structural order parameter and the strain ε_n (denoted as ε hereafter) along the applied compressional stress. Hence, G can be expanded as a power series in a single scalar order parameter Q . Sornette (2001) suggested a fourth-order equation:

$$G=bQ^4/4-aQ^2/2+fQ+dQ\varepsilon+\eta\varepsilon^2/2. \quad (5)$$

In Eq. (5), Q represents a pure dilational coupling or a pure shear coupling; b and a are two coefficients for the phase transition; f controls the breaking of symmetry between two phases; d quantifies the strength of the coupling between Q and ε ; and $\eta\varepsilon^2/2$ is the elastic energy of the material with $\eta=YV$ (Y =Young's modulus and V =stressed volume).

When $\varepsilon=0$, the critical transition occurs at $a=0$ and separates a phase with $Q=0$ (for $a<0$) from that with $Q\neq 0$ (for $a>0$) possessing the $Q\rightarrow -Q$ symmetry. When $a>0, f=0$, and $\varepsilon=0$, the two phases $Q_{\pm}=\pm(a/b)^{1/2}$ have the same free energy. The symmetry between Q and $-Q$ is broken by the presence of non-zero field parameter f . Keeping $a>0$, varying f is able to describe a first-order transition between the two phases Q_+ and Q_- with a jump in order parameter when f goes through zero.

During the earthquake rupture processes including the precursory procedure, strain is not null even though it is small in the precursory procedure. Hence, it is necessary to examine the influence of strain and coupling between Q and ε . Strain is considered as a basic ingredient in structural phase transitions because elastic strain coupling is the

dominant interaction between atoms and mineral cells in the transitions (Marais *et al.*, 1991; Salje, 1990; Bratkovsky *et al.*, 1995). For the sake of illustration, the stable undeformed mineral and the metastable phase are, respectively, represented by Q_+ and Q_- , which are associated with the two minima of $G(Q)$. Note that in this model positive $\varepsilon (>0)$ results in an increase of the symmetry-breaking field. Although other forms of coupling do not show such a direct equivalence, they have the same qualitative properties. When $\varepsilon > 0$, the two phases have their respective order parameters which are the solution of $dG/dQ=0$ (a condition associated with the extremum of G) with $d^2G/dQ^2 > 0$ (a stability condition for local minimum). From Eq. (5), the first condition gives the cubic equation

$$Q^3 + \alpha Q + \beta = 0, \quad (6)$$

where $\alpha = -a/b$ and $\beta = (f + d\varepsilon)/b$. There are three cases of solutions based on the value of $(\beta/2)^2 + (\alpha/3)^3$ (c.f., Selby, 1975) and the critical strain $\varepsilon^* = -(f/d) + 2(27)^{-1/2} a^{3/2}/b^{1/2} d$, which is the critical strain and independent on η . The three cases are:

(1) $(\beta/2)^2 + (\alpha/3)^3 < 0$ (i.e., $\varepsilon < \varepsilon^*$): Eq. (6) has three real roots, two of which are stable. This is the regime where the two phases Q_- and Q_+ are locally stable and the phase Q_+ with the highest free energy is metastable.

(2) $(\beta/2)^2 + (\alpha/3)^3 > 0$ (i.e., $\varepsilon > \varepsilon^*$): Eq. (6) has one real solution and two conjugate complex solutions. Only the real one has a physical meaning and corresponds to the unique stable phase.

(3) $(\beta/2)^2 + (\alpha/3)^3 = 0$ (i.e., $\varepsilon = \varepsilon^*$): Eq. (6) has three real roots of which at least two are equal. For this critical value ε^* of the strain, the metastable state Q_+ becomes unstable as $d^2G/dQ^2|_{Q_+}$ vanishes and transforms into the stable phase Q_- .

Due to a lack of real experimental values of the coefficients for granite, gabbro, etc., only some test values are used for exploring the effect of strain on proxy defect. Figure 6a shows three curves for dependence of ε^* on $a/b^{1/3} d^{2/3}$ (displayed by the solid curves) based on ε^* for three values of f/d that is a key factor in influencing the phase transition. Clearly, ε^* increases with $a/b^{1/3} d^{2/3}$ for fixed f/d and decreases with increasing f/d for fixed $a/b^{1/3} d^{2/3}$. Because of $\varepsilon^* > 0$, we have $f/d < 2(27)^{-1/2} (a/b^{1/3} d^{2/3})^{3/2}$. Figure 6b shows a curve for ε^* on $a/b^{1/3} d^{2/3}$ for a certain value of f/d . The curve separates the whole domain into two sub-domains of solutions. The upper domain increases with f/d ; while the lower one

decreases with increasing f/d . In Fig. 6b, along the curve with $\varepsilon=\varepsilon^*$ for condition 3, the metastable state Q_+ becomes unstable as $dG^2/dQ^2|_{Q_+}=0$ and transforms into the stable phase Q_- . On the lower part for each curve, i.e., $\varepsilon<\varepsilon^*$ for condition 2, the two phases Q_- and Q_+ are locally stable and the phase Q_+ with highest G is metastable. On the upper part for each curve, i.e., $\varepsilon>\varepsilon^*$ for condition 2, the real solution is related to a unique stable phase.

Figure 7 shows the plots of G versus Q for $f=0$ (in a solid line), $f=0.5$ (in a dashed line), and $f=1$ (in a dotted line) when $dQ\varepsilon$ and $\eta\varepsilon^2/2$ are not included. Note that the three values of f meet the above-mentioned inequality. All curves pass through the original point and show the double well configuration. When $f=0$, the (solid) curve is symmetric and Q_+ and Q_- are both in the individual stable states and thus the two phase have the same free energy. When $f>0$, the symmetry is broken. An increases in f from 0 to non-zero, G at Q_+ increases to $G+\delta G$ and thus Q_+ changes from a stable state to unstable one, and on the other hand G at Q_- decreases to $G-\delta G$ and thus Q_- becomes more stable. Finally, unstable Q_+ does transform to stable Q_- when f is increased. Since the strain is not included, Fig. 7 shows the condition without a loading stress. Nevertheless, Fig. 7 still exhibits the existence of proxy defect as well as the h^* when $f>0$. This shows the lowest dotted line as displayed in Fig.1 for the h^* when the rock sample is not under a loading stress. Of course, the quantity of h^* should be very small.

Figure 8 displays the plots of G/G_{max} versus Q for $a=2, 2.5,$ and 3.0 when $dQ\varepsilon$ and $\eta\varepsilon^2/2$ are included. Three value of a are taken for the left, middle, and right diagrams, respectively, In Fig. 8, the values of $b, f,$ and d are, respectively, 1, 1, and 1. The value of f meets the above-mentioned inequality. G_{max} is the maximum of all values of G in the three diagrams. Note that the presence of $\eta\varepsilon^2/2$ shifts all curved upward to make the curves be not able to pass through the original point, but this term cannot change the general pattern of a curve. In each of the three diagrams different lines represent distinct energy levels: the thin line for the regular energy level excluding strain, i.e., $\varepsilon=0$; the solid lines for those with $\varepsilon=\varepsilon^*$; the dashed lines for those with $\varepsilon>\varepsilon^*$; and the dotted lines for those with $\varepsilon<\varepsilon^*$. The values of ε^* are 0.633, 1.282, and 2.00, for left, middle, and right diagrams, respectively. Starting from a double well configuration (displayed by the thin curve) in which Q_- and Q_+ are both stable, the deformation applied to the rocks leads to the phenomena that the Q_- phase creates lower G , i.e., $G\rightarrow G-\delta G$ and $Q_-\rightarrow Q_--\delta Q$ (the

minimum shifting to the left); while the Q_+ phase creates higher G , i.e., $G \rightarrow G + \delta G$ and $Q_+ \rightarrow Q_+ + \delta Q$ (the maximum shifting to the right) which eventually becomes more higher than Q_- . The Q_+ phase is stable when $\varepsilon < \varepsilon^*$ (see the dotted curves), metastable when $\varepsilon = \varepsilon^*$ (see the solid curve), and unstable when $\varepsilon > \varepsilon^*$ (see the dashed curves). As the strain increases, the free energy landscape deforms until a point where Q_+ becomes unstable when $\varepsilon > \varepsilon^*$ and thus the phase transforms back into the Q_- phase. Thus, Fig. 8 suggests that when $\varepsilon < \varepsilon^*$, it is impossible to produce proxy defect; when $\varepsilon > \varepsilon^*$, it is easier to produce proxy defect that will increase with ε . This is consistent with the experimental results obtained by Freund and his co-authors.

3.3 The Depth Range for Producing Stress-induced Charges in a Fault Zone

Although the CE model sounds very significant for the studies of EM precursors, numerous basic problems arise. These problems include (1) the depth distribution of electric conductivity, C_e , or electric resistivity (R_e , an inverse of C_e); and (2) depth dependence of stresses. The depth distribution of C_e or R_e will be discussed in the next section. Here, we consider depth dependence of stresses. In addition, the fault zone is not straightly vertical as displayed in the CE model and the geometry of a fault depends on the faulting type. There are three faulting types: thrust, normal, and strike-slip faulting as displayed in Fig. 9. Each type has various dip angles ($< 60^\circ$) that are dependent on the static friction coefficient on a fault plane and commonly 45° – 62.5° for normal faults and 22.5° – 45° for thrust faults. Indeed, the strike-slip fault is usually not straightly vertical even though their dip angle may be large. The stresses exerted on the fault plane should depend on the dip angle. Hence, it is necessary to explore the effects due to dip angle and faulting type of a fault on the generation of stress-induced currents.

The detailed explanation about the geometrical structures of faults and mechanics of stresses can be seen in Turcotte and Schubert (1982) and Wang (2020) made a simple description. As displayed in Fig. 9, there are three stresses, σ_1 , σ_2 , and σ_3 loading on a fault. Two of them depending on faulting type are composed to produce the normal stress σ_n , which is perpendicular to the fault, and the shear stress σ_s , which is along the fault. For the CE model, the compressional stress is just the horizontal one, i.e., σ_1 , because the fault is straightly vertical. Note that the straightly vertical fault is very few and exists only

for some special strike-slip faults.

Although Freund and his co-authors only took normal pressures, σ_n , on the samples in their experiments, indeed σ_n and σ_s may both induce the mechanochemical processes on stressed rocks and the effect caused by σ_s is often stronger than that due to σ_n (Gilman, 1995). Nevertheless, in order to compare the experiments made by Freund and his co-authors, only σ_n is considered below. For thrust and normal faults, Wang (2020) obtained $\sigma_n = \sigma_L + \sigma_T [1 - \cos(2\theta)]/2 = \sigma_L + \sigma_T [1 - f_s/(1 + f_s^2)^{1/2}]/2$, where $\sigma_L = \rho g z$ is the lithostatic pressure at depth z , σ_T is the tectonic deviatoric stress, θ is the dip angle of the fault, and f_s is the static friction coefficient on the fault. For strike-slip faults, Wang (2020) gained $\sigma_n = \sigma_L - \sigma_T \cos(2\psi) = \sigma_L - \sigma_T f_s/(1 + f_s^2)^{1/2}$, where the fault is inclined at an angle ψ to the direction of σ_1 . The σ_T is $\pm 2f_s(\sigma_L - p_w)/[(1 + f_s^2)^{1/2} - (\pm f_s)]$ (the upper and lower signs of ‘ \pm ’ for thrust faults and normal faults, respectively) and $f_s(1 + f_s^2)^{1/2}(\sigma_L - p_w)/(1 - f_s^2)$ for strike-slip faults. In the two expressions, p_w is the pore fluid pressure. In general, f_s ranges from 0 to 0.85 and $p_w (= \lambda_v \sigma_L)$ is $\sim 0.4 \rho g z$.

Since σ_n increases with depth, z , it is impossible to take the value of σ_n at a certain depth to evaluate electric current. My strategy is to use the average, σ_{na} , of normal stresses loading on a fault in a depth range 0 to H (see Fig. 10) which is deep enough to gain a large enough value of σ_{na} being able to yield electric current. Considering $\lambda_v = 0.4$, H is calculated from the following formulas (Wang, 2020):

$$H = H_o / \{1 + 0.6[1 - f_s/(1 + f_s^2)^{1/2}]/f_s[(1 + f_s^2)^{1/2} - f_s]\}^{-1} \quad (7)$$

for thrust faults;

$$H = H_o / \{1 - 0.6[1 + f_s/(1 + f_s^2)^{1/2}]/f_s[(1 + f_s^2)^{1/2} + f_s]\}^{-1} \quad (8)$$

for normal faults; and

$$H = H_o / [(1 + 0.6f_s^2)/(1 - f_s^2)]^{-1} \quad (9)$$

for strike-slip faults. In Eqs. (7)–(9), $H_o = 2\sigma_{na}/\rho g$ is the depth at $f_s = 0$.

The gradient of σ_L with depth is ρg whose average value is ~ 27.5 MPa/km in the

Earth's crust (Turcotte and Schubert, 1982). For examples, H_o is ~ 727.2 m for $\sigma_{na}=10$ MPa, ~ 1818.0 m for $\sigma_{na}=25$ MPa, and ~ 4363.2 m for $\sigma_{na}=60$ MPa. Figure 11 shows the plots of H versus f_s with $\sigma_{na}=10, 25,$ and 60 MPa for three faulting types when $0.0 \leq f_s \leq 0.85$. In each diagram, two thin horizontal dotted lines display the permeability barrier (or transition layer), whose upper boundary has a depth of ~ 2000 m and the lower boundary has a depth range $3000\text{--}6000$ m for different areas (Zencher *et al.*, 2006), as displayed in Fig. 10. Considering $\sigma_{na}=10$ MPa, the depth range is $510.6\text{--}727.2$ m for thrust faults, $727.2\text{--}1263.1$ m for normal faults, and $582.4\text{--}727.2$ m for strike-slip faults. Considering $\sigma_{na}=25$ MPa, the depth range is $1276.4\text{--}1818.0$ m for thrust faults, $1818.0\text{--}3157.7$ m for normal faults, and $1456.7\text{--}1818.0$ m for strike-slip faults. Considering $\sigma_{na}=60$ MPa, the depth range is $3063.5\text{--}4363.2$ m for thrust faults, $4363.2\text{--}7518.2$ m for normal faults, and $3494.0\text{--}4363.2$ m for strike-slip faults. Obviously, the depth range is much wider for normal faults than for thrust and strike-slip faults. Since σ_T is negative for normal faults, a wider depth range is needed to yield a certain σ_{na} for normal faults than others.

Figure 11 implicates that the electric current generated in normal faults should be weaker than that in thrust and strike-slip faults, because a wider depth range is needed for the former than the latter. Hence, it is more difficult to generate EM precursors before earthquakes for normal faulting than for thrust and strike-slip faulting. In addition, for thrust and strike-slip faulting it is easier to generate the electric current for smaller f_s than that for larger f_s , because the depth range is wider for the former than the latter and increases with σ_n . The situation is opposite for normal faulting. Hence, for lower angle thrust and normal faulting it is easier to produce EM precursors for smaller θ than larger θ . For strike-slip faulting, it is easier to produce EM precursors for smaller ψ than larger ψ .

The average normal stress $\sigma_{na}=10$ MPa can yield, at least, $0.1 \mu\text{A}$ ground electric current as made by Freund *et al.* (2004). Its depth ranges are all shallower than 2000 m for three faulting types. This is a typical manner to generate stress-induced charges. The higher σ_n is, the wider the depth range is. Figure 11 exhibits that it is necessary to cover a wider depth range even including the permeability barrier to yield $\sigma_{na}>25$ MPa. Although this meets the requirement of the CE model, two problems arise. The first problem is that high λ_v in the permeability barrier leads to low σ_{Ta} and thus low σ_{na} . In order to produce a higher normal stress, there must be a wider depth range covering the

crust below the permeability barrier. The second problem will be explained in the next section. Together with the discussion given in the next section, Fig. 11 seems to suggest that $\sigma_{na}=25$ MPa is the upper limit for generation of typical stress-induced charges. The electric current generated in the uppermost 2 km crust is lower than that done in the crust as expected by Freund and their co-workers.

3.4 Electric Properties of Fault Zones

In order to meet the CE model, C_e must simply increase with depth or, at least, is higher in the lower crust than in the upper crust. From experimental results, Freund (2003, 2011) showed an increase in C_e with T and Freund (2010) reported an increase in C_e with σ . Since T and σ both increase with depth (Turcotte and Schubert, 1982), C_e increases with depth. In other word, R_e , (in Ohm-m or Ω -m), decreases with increasing depth. But, the results from numerous field surveys (e.g., Chen and Chen, 2000, 2002; Fujita *et al.*, 2004; Unsworth and Bedrosian, 2004; Morrow *et al.*, 2005; Nover, 2005; Seminsky *et al.*, 2016; Lu *et al.*, 2019) across the faults in different tectonic regions reveal that R_e increases with depth even though R_e is lower inside the fault zone than outside it. Obviously, laboratory experiments are not consistent to field surveys. One possible reason to cause such an inconsistency might be the use of dry or low-humidity rocks by Freund and his co-workers. Several studies (e.g., Seminsky *et al.*, 2016; Lu *et al.*, 2019; and cited references therein) suggested that in addition to T and σ , more factors may yield depth-increasing C_e or depth-decreasing R_e . These factors are: (1) an increase in water content or fractional volume of water that causes increases in degree of saturation pore fluids; (2) an increase in moisture content; (3) an increase in the salinity of pore fluids (representing the existence of more ions to conduct electricity); (4) an increase in the degree (or density) of fracturing of rocks (to create extra channels or to improve interconnection between pores for water currents); (5) an increase in clay minerals; and (6) a decrease in connection between pores under a constant fluid content. Compaction (to decrease the pathways for electric current flow) and lithofication (to block pores by deposition of minerals) may increase R_e . The above-mentioned six factors are not necessarily a function of depth. An increase in R_e with depth is not beneficial for the generation of stress-induced charges in the upper crust and the p-n transition in the lower crust.

Figure 11 reveals that the depth ranges of three faulting types for $\sigma_n=65$ MPa are almost below the uppermost crust and thus covering the permeability barrier (or transition layer). The phenomena also exist for $\sigma_n>25$ MPa. The electric properties are different in the hydrostatic layer and the permeability barrier. In Fig. 10, the transition from the hydrostatic layer to the permeability barrier generally is due to crustal deformations in the greenschist and higher grade metamorphic environments. The R_e values of the greenschist and higher grade metamorphic rocks are larger than those of the shallow fault-zone rocks which are mainly composed of gouges and breccias. Hence, R_e is larger in the permeability barrier than in the hydrostatic layer. This may reduce the ability of generating electric currents in the permeability barrier. Hence, the laboratory result that stronger σ_n produces a larger electric current cannot be directly applied to the real Earth's crust as suggested by the CE model.

4. Conclusions

To produce the electromagnetic precursors before an earthquake, the generation of electric currents on the ground surface or in the shallow depths of uppermost crust near the fault zone of the event is a necessary condition. Such currents could be generated due to the presence of stress-induced charges in the fault zone. From laboratory experiments, Freund (2002) proposed a peroxy defect theory to interpret the stress-induced charges in the experiments. Freund *et al.* (2006) proposed a critical- earthquake model to explain how the stress-induced electric currents flow in and near the hypocentral area of an earthquake. In this study, we explore such a theory based on mechanochemistry (Gilman, 1996). Stress-induced charges can be regarded as a kind of phase transition, which may be studied by using the Gibbs free energy (Gibbs, 1873): $G=U+pV-TS$ in which U , p , V , T , and S are, respectively, the internal energy, pressure, volume, temperature, and entropy. According to the Landau theory (Landau, 1937), for a structural transition G can be represented by a single order parameter function (see Sornette, 2001): $G=bQ^4/4-aQ^2/2+fQ+dQ\varepsilon+\eta\varepsilon^2/2$, in which Q is a scalar order parameter; a and b are two phenomenological coefficients for the phase transition; the coefficient f controls the breaking of symmetry between two phases; the coefficient d quantifies the strength of the coupling between Q and strain; and $\eta\varepsilon^2/2$ is the elastic energy of the material with Young's modulus Y times stressed volume, V . The solutions of this function are taken to

study the intrinsic properties of the model and the possibility of producing stress-induced charges. Preliminary results reveal that the G function shows a symmetric double-well configuration as $f=0$, $d=0$, and $\varepsilon=0$; the parameter f and d break the symmetry of the function; and $\eta\varepsilon^2/2$ will shift the configuration upward. An increase of ε will make the phase state change from the stable state, then the metastable state, finally to the unstable state. This may explain the generation of stress-induced charges on a rock under external loading. Results suggest that in addition to stress, the strain is also an important factor in influencing generation of charges. According to geometry and mechanics of stresses in the crust, for three faulting types the depth ranges for yielding an average normal stress which is able to generate a certain number of electric charges are estimated. The dip angle and faulting type of a fault can influence the depth ranges. The depth ranges are similar for thrust and strike-slip faults and narrower than those for normal faults. This suggests that for a certain depth range the ability of generating stress-induced charges is almost the same for thrust and strike-slip faults and lower for normal faults. The underground spatial distribution of resistivity or conductivity remarkably controls the generation of stress-induced charges and the flows of produced p-holes and electrons in the hypocentral area. The permeability barrier whose electric resistivity is higher than that of the uppermost crust may influence the generation of stress-induced charges.

Acknowledgments. The study was by the Central Weather Bureau (Grant No.: MOTC-CWB-109-E-02) and Academia Sinica, TAIWAN, ROC for financial support.

References

- Anderson DL (1989) Theory of the Earth. Blackwell Sci Pub Boston USA p 366
- Bratkovsky AM, Salje EKH, Marais SC, Heine V (1995) Strain coupling as the dominant interaction in structural phase transition. *Phase Transition* 55:79-126
- Chen CC, Chen CS (2002) Sanyi-Puli conductivity anomaly in NW Taiwan and its implication for the 1999 Chi-Chi earthquake. *Geophys Res Letts* 29(8) 10.1029/2001GL013890.
- Chen CS, Chen CC (2000) Magnetotelluric soundings of the source area of the 1999 Chi-Chi earthquake in Taiwan: Evidence of fluids at the hypocenter. *Terr Atmos Ocean Sci* 11(3):679-688.

- Freund F (1985) Conversion of dissolved 'water' into molecular hydrogen and peroxy linkages. *J Non-Cryst Solids* 71(1-3):195-202 DOI:10.1016/0022-3093(85)90288-1
- Freund F (2000) Time-resolved study of charge generation and propagation in igneous rocks. *J Geophys Res Solid Earth* 105(B5):11001-11019 doi:10.1029/1999JB900423
- Freund F (2002) Charge generation and propagation in igneous rocks. *J Geodyn* 33: 543-570 doi:10.1016/S0264-3707(02)00015-7
- Freund F (2003) On the electrical conductivity structure of the stable continental crust. *J Geodyn* 35:353-388
- Freund F (2007b) Pre-earthquake signals – Part II: Flow of battery currents in the crust. *Nat Hazards Earth Syst Sci* 7:543-548
- Freund F (2010) Toward a unified solid state theory for pre-earthquake signals. *Acta Geophys* 58(5):719-766 doi:10.2478/s11600-009-0066-x
- Freund F (2011) Pre-earthquake signals: Underlying physical processes. *J Asian Earth Sci* 41:383-400
- Freund F (2013) Earthquake forewarning – A multidisciplinary challenge from the ground up to space. *Acta Geophys* 61(4):775-807 doi:10.2478/s11600-013-0130-4
- Freund F, Freund M (2015). Paradox of peroxy defects and positive holes in rocks Part I: Effect of temperature. *J Asian Earth Sci* 114:373-383 doi:10.1016/j.jseaes.2015.04.047
- Freund F, Masuda M (1991) Highly mobile oxygen hole-type charge carriers in fused silica. *Mater Res* 6(8):1619-1622, <http://dx.doi.org/10.1557/JMR>. 1991.1619
- Freund F, Sornette D (2007) Electromagnetic earthquake bursts and critical rupture of peroxy bond networks in rocks. *Tectonophys* 431:33-47
- Freund F, Wengeler H (1982) The infrared spectrum of OH-compensated defect sites in C-doped MgO and CaO single crystals. *J Phys Chem Solids* 43:129-145
- Freund F, Takeuchi A, Lau BWS (2006) Electric currents streaming out of stressed igneous rocks – A step towards understanding pre-earthquake low frequency EM emissions. *Phys Chem Earth* 31(4-9):389-396 DOI:10.1016/j.pce.2006.02.027
- Freund F, Wengeler H, Martens R (1982) A hydrogen-deuterium fractionation mechanism in magnesium oxide. *Geochim Cosmochim Acta* 46:1821-1829
- Freund F, Takeuchi A, Lau BWS, Post R, Keefner J, Mellon J, Al-Manaseer A (2004)

- Stress-induced changes in the electrical conductivity of igneous rocks and the generation of ground currents. *Terr Atmos Ocean Sci* 15(3):445-475
- Fujita K, Katsura T, Tainosho Y (2004) Electrical conductivity measurement of granulite under mid- to lower crustal pressure–temperature conditions. *Geophys J Int* 157:79-86
- Gibbs JW (1873) A method of geometrical representation of the thermodynamic properties of substances by means of surfaces. *Transactions of the Connecticut Academy of Arts and Sciences* 2:382-404
- Gilman JJ (1995) Mechanism of shear-induced metallization. *Czech J Phys* 45(12): 913-919
- Gilman JJ (1996) Mechanochemistry. *Science* 274:65
- Kuo CL, Huba JD, Joyce G, Lee LC (2011) Ionosphere plasma bubbles and density variations induced by pre-earthquake rock currents and associated surface charges. *Geophys Res* 116 A10317 doi:10.1029/2011ja016628
- Kuo CL, Lee LC, Huba JD (2014) An improved coupling model for the lithosphere-atmosphere-ionosphere system. *Geophys Res Space Phys* 119:3189-3205 doi:10.1002/2013JA019392
- Landau L (1937) On the theory of phase transitions. *Zh Eks Teor Fiz* 7 19-32
- Lu Y, Abuel-Naga H, Rashid QA, Hasan MF (2019) Effect of pore-water salinity on the electrical resistivity of partially saturated compacted clay liners. *Adv Mater Sci Engin* Article ID 7974152 p 13 <https://doi.org/10.1155/2019/7974152>
- Marais S, Heine V, Nex C, Salje E (1991) Phenomena due to strain coupling in phase transitions. *Phys Rev Lett* 66 2480-2483
- Morrow C, Lockner DA, Hickman S (2005) Low resistivity and permeability in actively deforming shear zones on the San Andreas Fault at SAFOD. *J Geophys Res Solid Earth* 120:8240-8258 doi:10.1002/2015JB012214
- Namgaladze AA, Zolotov OV, Karpov MI, Romanovskaya YV (2012) Manifestations of the earthquake preparations in the ionosphere total electron content variations. *Nat Sci* 4(11):848-855 doi:10.4236/ns.2012.411113
- Nover G (2005) Electrical properties of crustal and mantle rocks – a review of laboratory measurements and their explanation. *Surv Geophys* 26(5):593- 651
- Ouzounov D, Pulinets S, Hattori K, Taylor P (eds) (2018) *Pre-Earthquake Processes: A Multidisciplinary Approach to Earthquake Prediction Studies*. AGU publication p 384

- Pulinets S, Ouzounov D (2011) Lithosphere–Atmosphere–Ionosphere Coupling (LAIC) model – An unified concept for earthquake precursors validation. *J Asian Earth Sci* 41(4/5):371-382 doi:10.1016/j.jseaes.2010.03.005
- Reif F (1965) *Fundamentals of statistical and thermal physics*. McGraw-Hill New York USA p 651
- Salje EKH (1990) *Phase Transitions in Ferroelastic and Co-elastic Crystals: An Introduction for Mineralogists, Material Scientists, and Physicists*. Cambridge Univ Press London p 366
- Scholz CH (1990) *The Mechanics of Earthquakes and Faulting*. Cambridge Univ Press Cambridge p 439
- Scoville J, Heraud J, Freund F (2015) Pre-earthquake magnetic pulses. *Nat Hazards Earth Syst Sci* 15(8):1873-1880
- Selby SM (1975) *CRC Standard Mathematical Tables and Formulae*. 21th Edition The Chemical Rubber Co p 724
- Seminsky KZh, Zaripov RM, Olenchenko VV (2016) Interpretation of shallow electrical resistivity images of faults: tectonophysical approach. *Russian Geol Geophys* 57:1349-1358
- Shluger AL, Heifets EN, Gale JD, Catlow CRA (1992) Theoretical simulation of localized holes in MgO. *J Phys Condens Matter* 4:5711-5722
- Sibson RH (1977) Fault rocks and fault mechanisms. *J Geol Soc Landon* 133: 191-21.
- Sibson RH (1992) Implications of fault-valve behavior for rupture nucleation and recurrence. *Tectonophys* 211:283-293
- Sornette D (1999) Earthquakes: from chemical alteration to mechanical rupture. *Phys Rep* 313:237-291
- Sornette D (2001) Mechanochemistry: An hypothesis for shallow earthquakes. In: Teisseyre R, Majewski E (eds.) *Earthquake Thermodynamics and Phase Transformation in the Earth's Interior* 1st Edition Cambridge Univ Press p 674
- Turcotte DL (1991) Earthquake prediction. *Annu Rev Earth Planet Sci* 19:263-281
- Turcotte DL, Schubert G (1982) *GEODYNAMICS – Applications of Continuum Physics to Geological Problems*. Wiley p 450.
- Unsworth MJ, Bedrosian PA (2004) On the geoelectric structure of major strike-slip faults and shear zones. *Earth Planets Space* 56:1177-1184
- Wang JH (2020) Piezoelectricity as a mechanism on generation of electromagnetic

precursors before earthquakes. Geophys J Int (in press)

Weidendorfer D, Schmidt MW, Mattsson HB (2017) A common origin of carbonatite magmas. *Geology* 45(6):507-510 doi:10.1130/G38801.1

Zencher F, Bonafede M, Stefansson R (2006) Near-lithostatic pore pressure at seismogenic depths: a thermoporoelastic model. *Geophys J Int* 166:1318-1334

Zolotov OV, Namgaladze AA, Zakharenkova IE, Martynenko OV, Shagimuratov II (2012) Physical interpretation and mathematical simulation of ionospheric precursors of earthquakes at midlatitudes. *Geomagn Aeron* 52(3):390-397 doi:10.1134/S0016793212030152

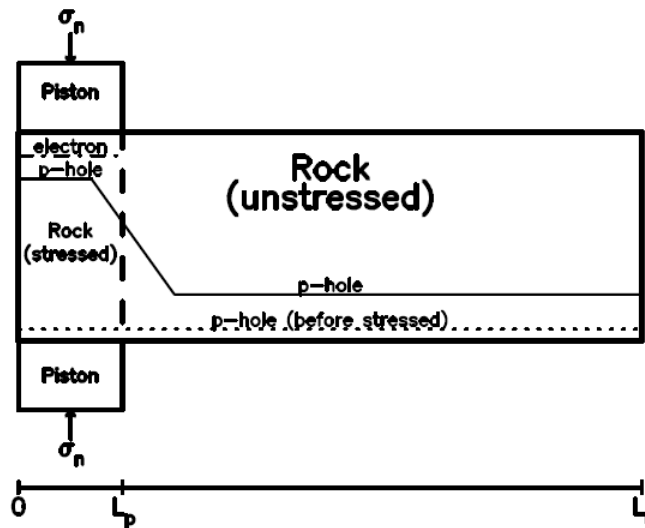


Figure 1. Black diagram of the uniaxial compression tests: granite slab. The granite slab (1.2 m long, $10 \times 15 \text{ cm}^2$ cross section) is fitted with two Cu electrodes (each $30 \times 15 \text{ cm}^2$), one at the back end and one at the front end, plus a non-contact capacitive sensor for measuring the surface potential. The rock is insulated from the pistons and the press by 0.8 mm thick polyethylene sheets ($>10^{14} \Omega\text{-cm}$). Before application of stress the h^\bullet concentration is low and uniform throughout the rock (dashed line). After application of stress the concentration of e' and h^* increases in the stressed rock volume (dot-dashed). The h^* flows out, thus causing the h^* concentration in the stressed rock decrease and in the unstressed rock to increase (dotted). The unstressed rock becomes positively charged relative to the stressed rock. (modified from Freund and Freund, 2015)

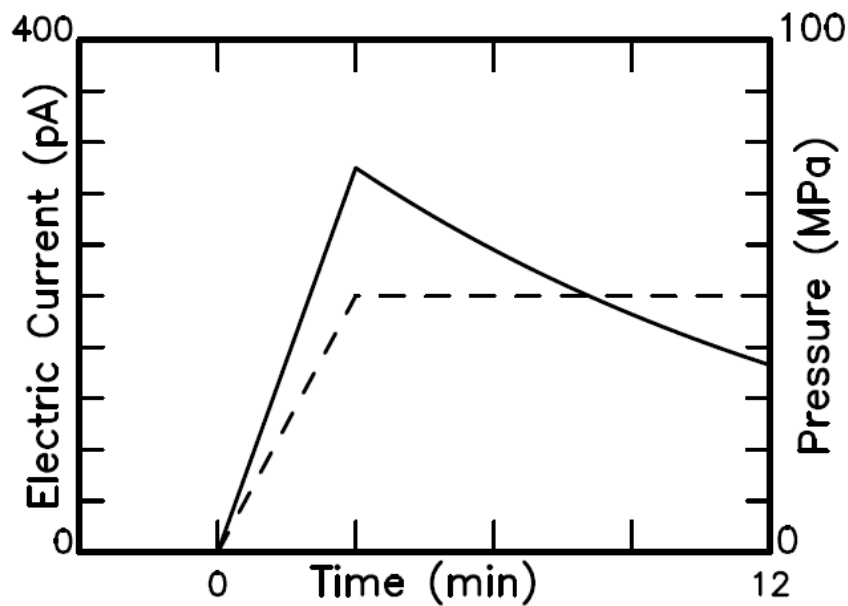


Figure 2. A characteristic feature of the stress-activation of charge carriers in rocks (displayed by solid lines) is a rapid increase of the outflow current which includes the intense current fluctuations during the early phase when the rock is loaded at a constant rate. The temporal variation in pressure is exhibited by dashed lines. (This figure schematically summarizes the experimental results obtained by Freund and his co-authors.)

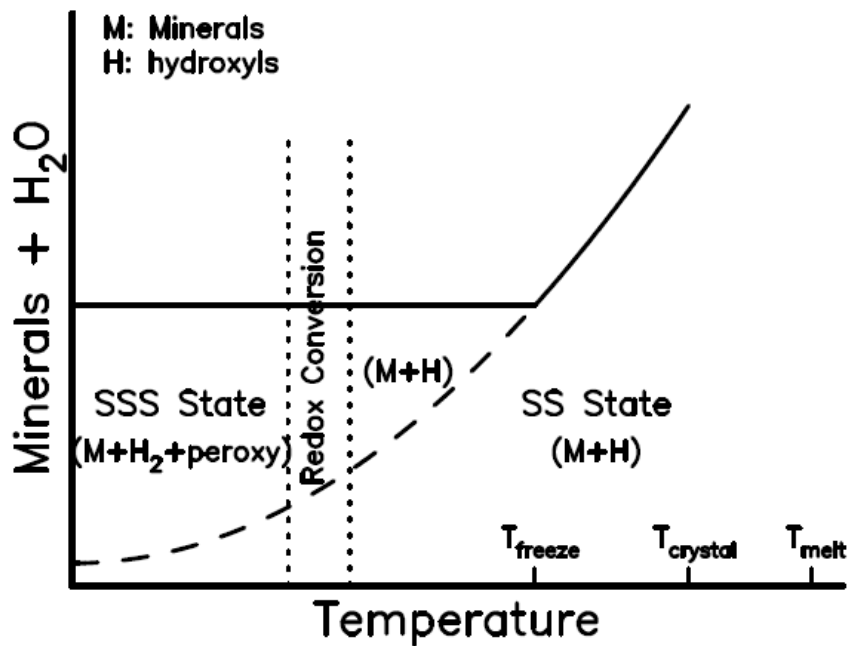


Figure 3. Part of a 2-component phase diagram “Mineral+H₂O”, indicating that the melting point of the dry system T_{melt} is lowered to the crystallization temperature, T_{cryst} , through formation of a solid solution (SS). The SS stability field shrinks with decreasing temperature. At T_{freeze}

the system freezes and leaves thermodynamic equilibrium. At this point, SS turns into a supersaturated solid solution, SSS. In the SSS field, a redox conversion takes place during further cooling, converting pairs of solute OH^- into peroxy plus H_2 . (modified from Freund and Freund, 2015)

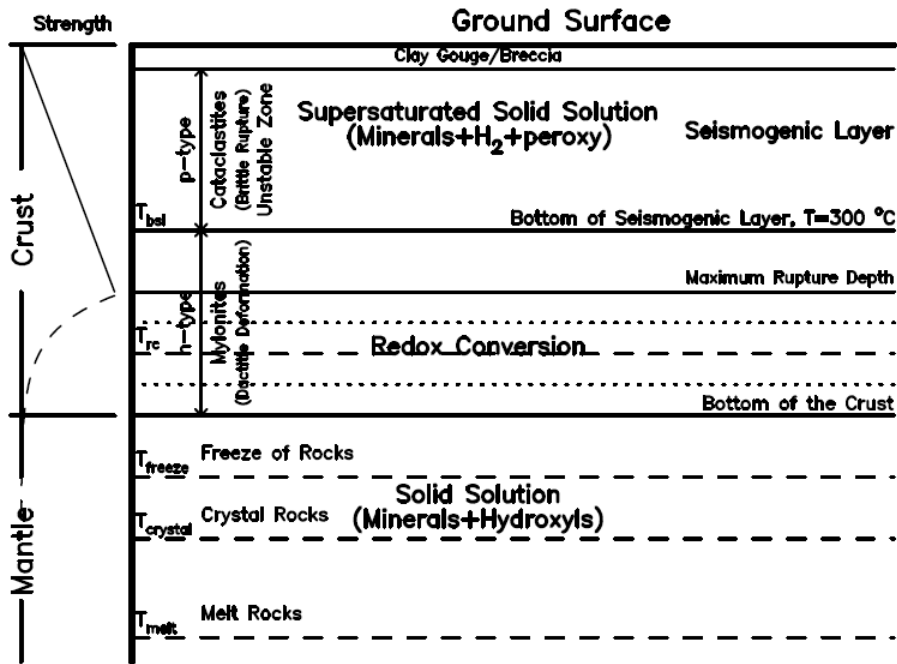


Figure 4. Vertical profile of subsurface geological structures, the bottom of seismogenic zone, the bottom of the crustal, and related information as described in the text.

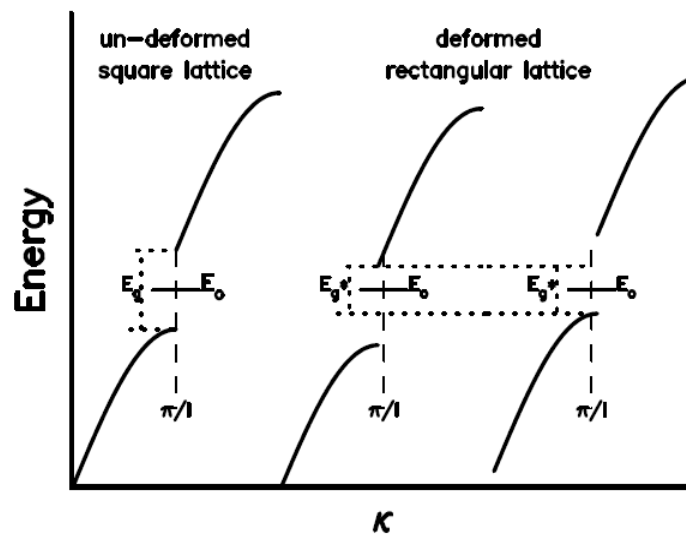


Figure 5. The plot of energy versus wavenumber for the states of nearly-free-electrons in a square atomic lattice of spacing “ l ”. The undeformed square lattice is shown on

the left. Simple shear converts it into a rectangle with axes $=l \pm \delta$ where δ is small but finite. The deformed rectangular lattices are shown on the middle and left. To a first approximation this does not change the gap, but it shifts it on the energy scale thereby decreasing the minimum gap. (modified from Gilman, 1995)

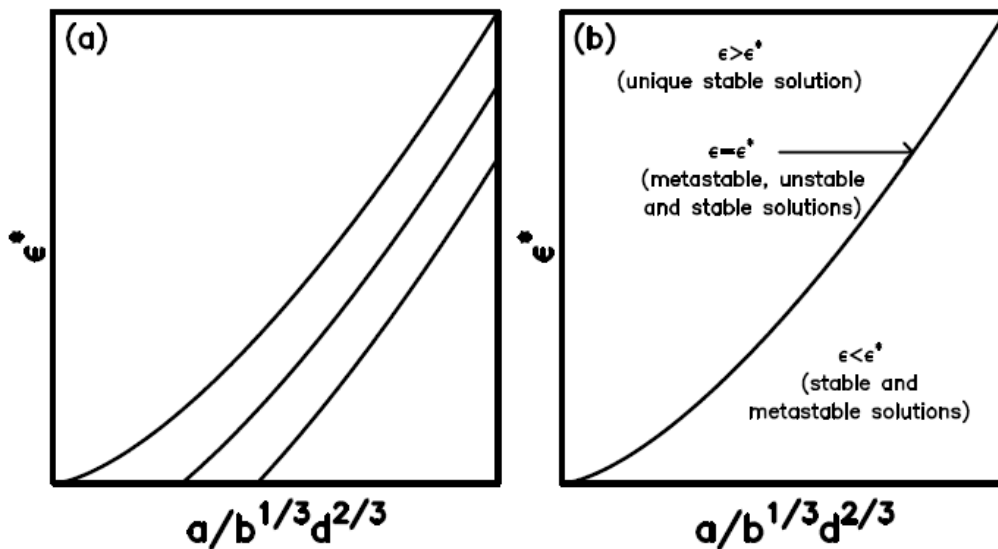


Figure 6. (a) The curves of dependence of ϵ^* with $a/b^{1/3}d^{2/3}$ for varying f/d .; and (b) a curve of ϵ^* in terms of $a/b^{1/3}d^{2/3}$ for a certain f/d and the curve separate the whole domain into two sub-domains of solutions.

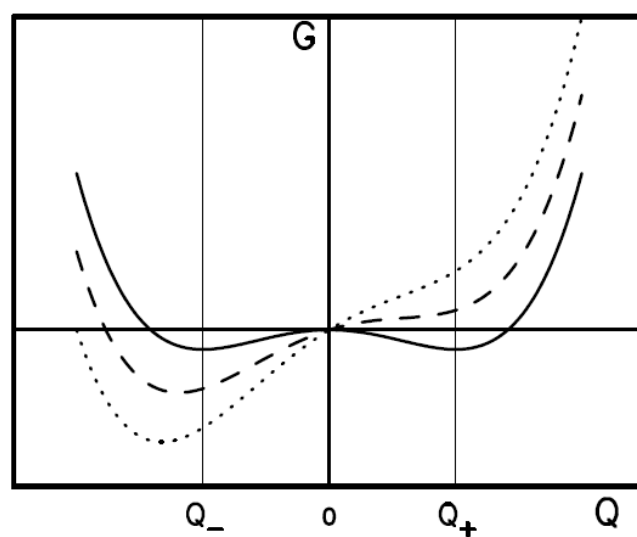


Figure 7. Figure displays the changes of energy levels depending on f when $a=2, b=1,$ and $d=1$: the solid line for $f=0.0$, dashed line for $f=0.5$, and dotted line for $f=1.0$. Q_+

and Q_- represent, respectively, the stable un-deformed phase and the metastable phase of rocks and are associated with the two minima of G in terms of Q . The left and right thin vertical lines represent Q_- and Q_+ , respectively.

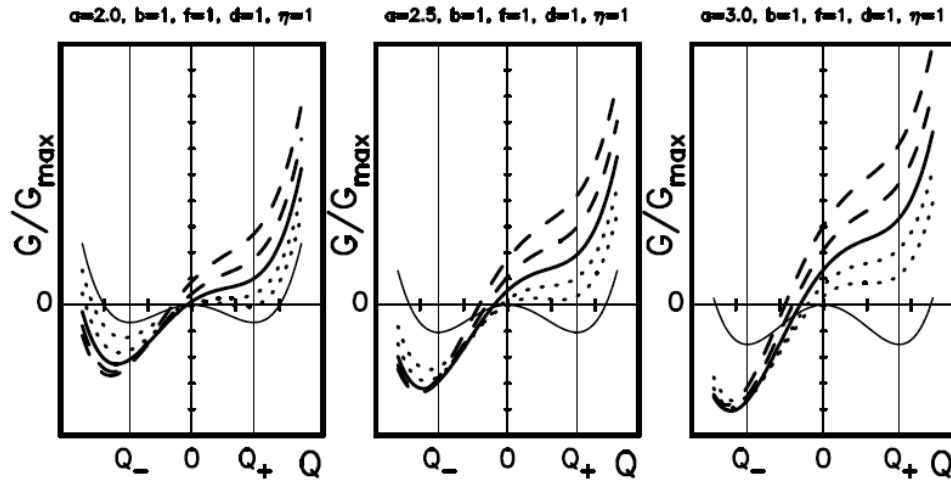


Figure 8. Figure displays G/G_{max} ($G_{max}=\max|G|$ in the three diagrams) versus Q : the thin lines in the three diagrams representing the regular energy level excluding strain, i.e., $\varepsilon=0$; the solid lines for $\varepsilon=\varepsilon^*$; the dashed lines for $\varepsilon>\varepsilon^*$; and the dotted lines for $\varepsilon<\varepsilon^*$. The left and right thin vertical lines represent, respectively, the positions of Q_- and Q_+ , which are associated with the minimum values of G when $f=0$ and $d=0$.

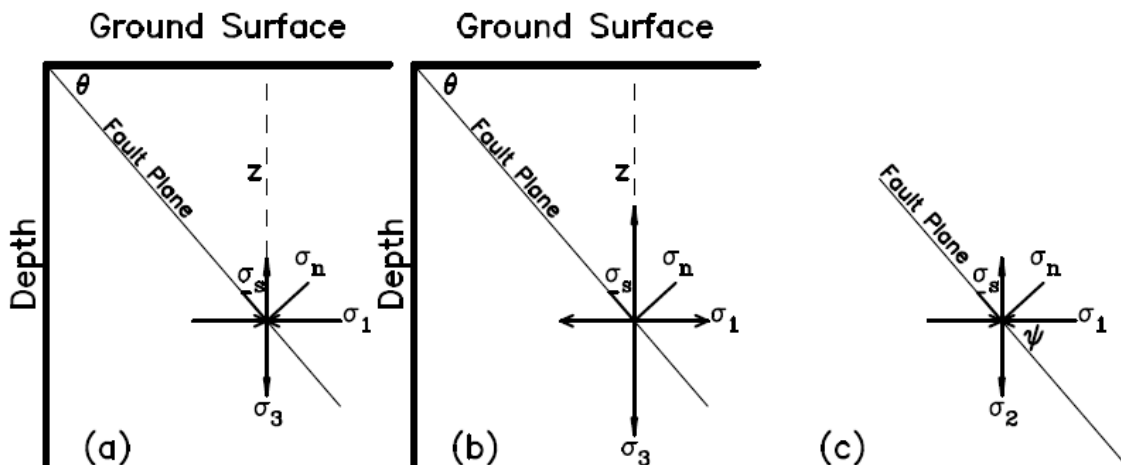


Figure 9. The geometrical structures of stresses for three types of faults: (a) for thrust fault, (b) for normal fault, and (c) for strike-slip fault. The depth is denoted by z . The principal stresses along the horizontal vertical axes are $\sigma_1 (= \rho g z)$ and σ_3 , respectively. The σ_n and σ_s represent the normal stress and shear stress, respectively. The thrust

and normal faults have a dip angle of θ . The strike-slip fault is inclined to the direction of σ_1 is ψ .

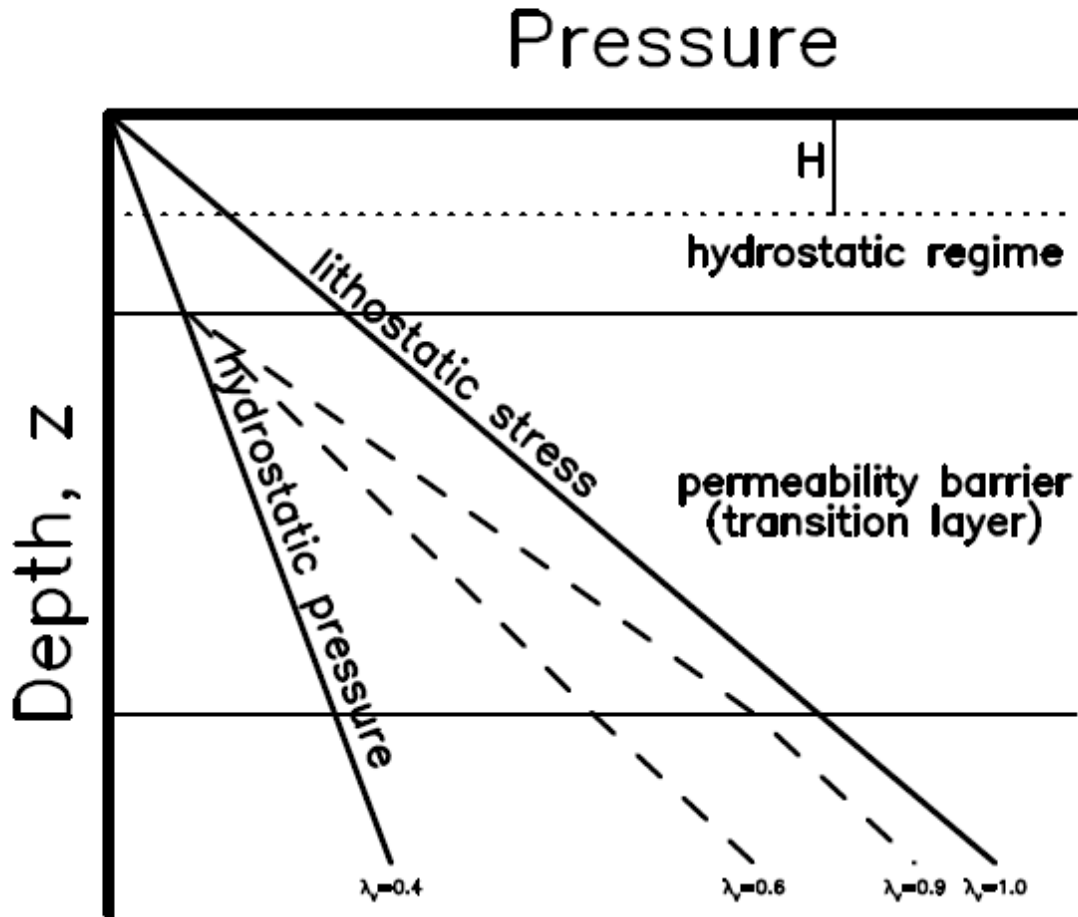


Figure 10. Schematic diagram for underground stress system: the right inclined line representing the depth-increasing lithostatic stress, the left line denoting the depth-increasing hydrostatic pressure with $\lambda_v=0.4$; two dashed lines showing two examples ($\lambda_v=0.6$ and 0.9) of increases in hydrostatic pressures due to the permeability barrier or transition layer which is located in between two horizontal lines (see the text). The depth range in between the ground surface and a depth of H expresses the range within which the loaded stress can yield the strong enough electric field for generating EM precursors as discussed in the text. (modified from Sibson (1977) and Zencher et al. (2006))

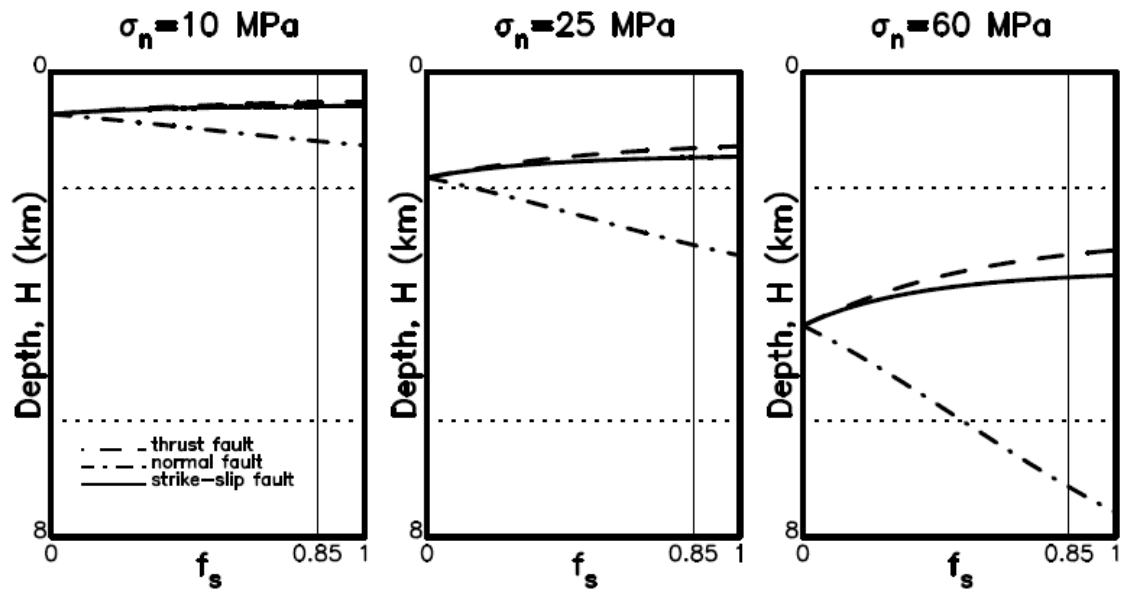


Figure 11. The plots of H versus f_s for three values of σ_{na} , i.e., 10, 25, and 60 MPa, and for three faulting types: a dashed line for thrust fault, a dashed-dotted line for normal fault, and a solid lines for strike-slip fault. The thin vertical line represents $f_s=0.85$. The two horizontal lines show the permeability barrier or transition layer as displayed in Figure 10.